A multiscale study of the production and recombination of closely correlated defects from irradiation-induced higher order recoils in beryllium

Ch. Stihl[a], R. Kumar[b], P. V. Vladimirov[a], A. Möslang[a]

[a]*Karlsruhe Institute of Technology, 76344, Eggenstein-Leopoldshafen, Germany*
[b]*India Institute of Technology Roorkee, Uttarakhand 247667, India*

Abstract

Beryllium is considered as a neutron multiplier in the self-sustained fuel cycles of future fusion reactors like ITER and DEMO, thus the retention of tritium generated in transmutation events in beryllium is crucial for the operational safety of such devices. As tritium readily interacts with microstructural defects produced under neutron irradiation, its retention depends on the evolution of the microstructure. Thus, physics-based models to understand and ultimately predict the tritium retention behavior have to comprise the generation and recombination dynamics of such defects. Therefore, the generation and recombination of the most simple defects, i.e. closely correlated as well as separated Frenkel pairs, as produced at the very end of collision cascade branches are considered in this work. To that end, DFT calculations are performed to determine threshold displacement energies, typical closely correlated pair configurations, the volume of spontaneous recombination, and recombination energy barriers. On the basis of these atomic-scale results, rate-based recovery models are derived to simulate electrical resistivity recovery experiments. The proposed models suggest that the principal recovery peak of beryllium is associated with the onset of intra-basal self-interstitial diffusion. This association is found to hold for the principal recovery peak of zirconium as well and it is thus concluded it is likely to generalize to many hcp metals with smaller than ideal c to a ratios.

Keywords: ab initio, first principles, beryllium, molecular dynamics, DFT, electrical resistivity recovery

1. Introduction

Beryllium is proposed as a plasma facing material of the first wall [1] and a neutron multiplier in tritium-breeding blanket concepts [1, 2, 3] of future fusion devices like ITER and DEMO. To achieve a self-sustained fuel cycle, the inevitable loss of neutrons from undergoing processes not contributing to tritium breeding must be compensated by means of a neutron multiplier. The helium-cooled pebble bed (HCPB) blanket design comprises lithium ceramics as the actual tritium-breeding material and beryllium as a neutron multiplier. Highly energetic neutrons emitted from the fusion plasma result in numerous fast recoil primary atoms launching displacement cascades. Eventually, the neutrons trigger transmutation reactions in beryllium resulting in the production of tritium and helium [4]. Both processes have pronounced effects on the microstructure and mechanical properties of beryllium [5].

Conventionally, the number of displaced atoms $N(E_0)$ created by a primary recoil atom with kinetic energy E_0 is roughly approximated by

$$N(E_0) = 0.8 \frac{E_0}{2E_d}, \qquad (1)$$

with the minimal energy needed to displace an atom from its ideal lattice site E_d. This approximation is well known

as the Norgett-Robinson-Torrens formulation [6] which effectively takes the slow down of moving atoms into account.

Computationally, the rate of point defect production by a primary knock-on atom (PKA) is commonly computed by binary collision (BC) codes, e.g. SRIM [7], or molecular dynamics (MD). Although MD and BC approximations typically agree on the dependence between the created point defects and the kinetic energy of the PKA, the latter requires an explicit choice of E_d as a free parameter in order to obtain realistic predictions from eq. (1). Hence, a good approximation of the effective threshold energy E_d is required.

Computing such threshold energies from detailed, atomistic simulations considering crystallographic anisotropy can result in estimations quite different from the defaults used in BC codes like SRIM. MD calculations are being used routinely to study the effects of crystallographic anisotropy effects by sampling the space of crystallographically non-equivalent directions. Such calculations have been undertaken for a number of different materials, e. g., Fe [8, 9] and FeCr [10]. To obtain a single, representative value as an effective threshold displacement energy E_d, an expectation value is needed to be calculated in a non-trivial way. The matter is complicated by the probabilities of defect production not necessarily being simple single-step functions from zero to one and the need of an appropriate weighting choice for such sampled data [8, 11] in the respective directions. The pronounced importance of finding appropriate values even motivated experimental work directly accessing damage production in specific crystallographic direc-

tions [12, 13].

The main hurdle to take for MD calculations is to faithfully reproduce the physics of collisions at high velocities, i.e. those caused by the primary recoil. While a precise representation of these interactions are readily available when using density functional theory (DFT) based *ab initio* codes, the high computational costs going along with those codes impose narrow limits on feasible simulation sizes and times. Unfortunately, primary recoils along closed-packed directions tend to produce widely separated pairs of vacancies and interstitial atoms already just above the corresponding threshold displacement energy [11]. Together with simulation sizes constrained by computational cost, this indicates a tough trade-off when considering DFT-based studies of such processes. There are processes, which are well within the limits of what is feasible to be examined using DFT based simulations, though. Fortunately, examples of such processes are generation and recombination of closely correlated vacancy and interstitial pairs due to their comparatively compact spacial dimensions. These defect types are commonly considered to be the explanation for the onset of electrical resistivity recovery [14] on post-irradiation annealing. The spectra of such experiments are routinely used to gather insights into what kind of defects are created under irradiation and what are the conditions and microscopic processes that heal the respective damage. Ultimately, the presence of these defects are decisive factors in the assessment of tritium retention and release behavior of beryllium by means of predictive physics-based models as they will have to incorporate such defects as tritium traps.

Therefore, this work is concerned with investigating the generation and recombination of closely correlated pairs by means of DFT computations and a subsequent development of recovery models incorporating all these findings.

2. Computational methods

The rate equation model of recovery by Frenkel pair recombination is based on the collective findings of three routinely applied computational methods based on density functional theory. Details are given in the respective subsections below. The DFT-based computational methods applied in this work are microcanonical *ab initio* molecular dynamics (AIMD), structural optimization, and saddle point configuration searches by means of a climbing string method [15]. All calculations have been performed using VASP [16, 17] 5.4.1, the input to all of which has been handled using the "pymatgen" framework [18]. In general, all employed k-point grids are Γ-centered and at least as dense as a $31 \times 31 \times 31$ grid in the Brillouin zone of the conventional beryllium unit cell. The PAW [19, 20] GGA pseudopotential approximating exchange and correlation contributions as suggested by Perdew and Wang [21] with two free electrons was used to model beryllium in all computations. Furthermore, a second order Methfessel-Paxton [22] function on a width of $\sigma = 0.2$ was used to smear out the occupancy step at the Fermi energy level. All calculations were done with configurations consisting of at least 128 beryllium ions in a super-

structure of $4 \times 4 \times 4$ unit cells. Depending on characteristics of particular calculations, like the supplied recoil momentum or the configuration of the examined Frenkel pair, the simulation cells were modified to comprise $4 \times 4 \times 5$, $5 \times 5 \times 4$, or even to $6 \times 6 \times 3$ unit cells to avoid spurious interactions with periodic images. Additional algorithmic parameters or deviations from these defaults are reported in detail at the beginning of their respective subsections below.

2.1. Microcanonical ab initio molecular dynamics

All AIMD calculations were performed with a 250 eV plane wave cut-off energy, a "PREC" setting of "Low", and at 0 K. The time step as given by the "POTIM" tag was adjusted such that the projectile, and thus the fastest ion ever, travels 0.1 Å between the first and the second force evaluation. To ensure a sufficiently long trajectory, MD runs were carried out until a certain threshold of iterations, supplied via the "NSW" tag, were computed. This "NSW" value was adjusted such that the product of "NSW" and "POTIM" is kept at a constant value taken from a calculation carried out earlier, which evidently produced a defect. As a measure of validity, the microcanonical MD runs were routinely checked for conservation of energy monitoring the sum of kinetic and potential energy at every iteration.

2.2. Structural optimizations

The plane wave cut-off energy "ENCUT" was generally set to 450 eV and the "PREC" tag was set to "Normal" for structural optimizations. The electronic self-consistency convergence criterion as supplied by "EDIFF" was set to 10^{-4}. The supplied "EDIFFG" parameter results in configurations considered converged once the maximal ion force falls below $5.0 \cdot 10^{-3}$ eV/Å.

When starting from the last iteration of an AIMD simulation, relaxations were started using the conjugate-gradient descent with "IBRION" set to 2 and "POTIM" set to 0.5. If a relaxation did not readily converge, it was resumed using the quasi-Newton algorithm by setting "IBRION" to 1. When a symmetry is apparent in a converged configuration, these symmetries were perturbed by displacing a single ion by 0.025 Å in an appropriate direction. Starting from such disturbed configurations, a subsequent relaxation with more precise convergence settings of "EDIFF" and "EDIFFG" resulting in $1.0 \cdot 10^{-5}$ eV and $1.0 \cdot 10^{-3}$ eV/Å, respectively, was carried out. Only configurations either returning to their prior, high-symmetry configurations or to some other defect configuration different from the perfect crystal were considered candidate stable defect configurations.

When investigating recombination radii, configurations of ideal basal-octahedral (BO) interstitial Be and a single vacant lattice site with increasing distances in between were initialized within a symmetrically irreducible wedge of the perfect Be crystal. Subsequent relaxations with "EDIFFG" set to convergence under $1.0 \cdot 10^{-3} eV$/Å generally either result in a stable defect configuration or the reemergence of the perfect Be crystal. In the former case, the respective configuration is found to be part of the hull of smallest possible, stable Frenkel pairs of

BO interstitials around a central vacancy. In the latter case, the distance is deemed to be too short and thus the respective configuration is found to be within the volume around a vacancy, within which spontaneous recombination occurs.

2.3. Climbing string method saddle point searches

The settings deployed in these calculations generally align with those of the structural optimization described above with just a few exceptions. As usual when using VTST implementations, the ionic evolution of VASP was effectively switched off by setting "IBRION" to 3 and "POTIM" to 0.0. Thus, instead of any of the ionic algorithms provided by VASP itself, the steepest descent optimizer was used by supplying 4 for the "IOPT"-tag. Along with this choice of "IOPT", "SDALPHA" was set to ≥ 0.02 and "MAXMOVE" was ≤ 0.1 to scale the applied steps resulting form the forces. Typically, the full string with two or more images crudely converged with a more tolerant "EDIFFG" setting, before only the saddle point configuration was converged down to forces $\leq 0.01 \frac{eV}{\text{Å}}$.

Other than these choices, our CSM implementation requires some additional algorithmic parameters. All calculations were done with NEB-like nudging, which distributes the images in a roughly equidistant manner along the string by introducing artificial forces parallel to the string. To control the ascent of the string out of the energy well, the force component parallel to the string tangent was fully inverted, preserving the original magnitude of the full force. The initial configurations were generally chosen as configurations slightly displaced from the stable minimum along a rough approximation of the hyperdirection in which the minimal energy path ending in the saddle point configuration associated with the recombination process of interest is expected to start.

2.4. Rate-equation based recovery model

Chemical rate equations describe temporal evolution of the considered component's concentrations. The total concentration is preserved, as each process only converts one component into another, balancing any loss with a respective gain. The set of tracked components and processes converting them into each other can be considered as the sets of vertices and edges of a directed graph, respectively. Thus, our rate equation-based recovery model is implemented as a simple wrapper around the "MultiDiGraph" data structure of the "networkx" package [23], which provides a directed graph with parallel edges as a data structure in python. The wrapper allows to derive arbitrary rate equations in a flexible manner. Each considered physical process rate r_i is given as an Arrhenius-like function of the form

$$r_i(\vec{c}, \nu_i, \Delta E_i, t) = f(\vec{c}(t)) \nu_i \exp\left(-\frac{\Delta E_i}{k_B T(t)}\right) \qquad (2)$$

with an appropriate function $f(\vec{c}(t))$ of the current concentrations $\vec{c}(t)$, an attempt frequency ν_i, an energy barrier ΔE_i, and a temperature function of time $T(t)$. From these rates, the wrapper constructs a total time derivative for each vertex, and thus

component c in $\vec{c}$, by generating a coupled system of equation of the form

$$\frac{dc(\vec{c}, t)}{dt} = \sum_{i \in E_I^c} r_i(\vec{c}, \nu_i, \Delta E_i, t) - \sum_{o \in E_O^c} r_o(\vec{c}, \nu_o, \Delta E_o, t) \qquad (3)$$

with the sets of incoming and outgoing edges E_I^c and E_O^c at the vertex representing c, respectively. With given initial values $\vec{c}_0$ and the temperature function $T(t)$, the wrapper supports integration of the resulting system of coupled ordinary differential equations using a backward differentiation formula-based ODE solver as implemented in scipy [24]. The selected temperature function driving the physical process rates approximates the series of heating cycles in an actual electrical resistivity recovery experiment [14]. Each heating cycle consists of a heating time period t_h within which the temperature increases from T_0 to T obeying a heating function f_h, a holding time period t_T within which the temperature is kept at T, and a cooling time period t_c within which the temperature drops back from T to T_0 obeying a cooling function f_c. Thus, each cycle is approximated by

$$T(t) = \begin{cases} (T - T_0) \cdot f_h(t) + T_0 & 0 \leq t < t_h \\ T & t_h \leq t < t_h + t_T \\ (T - T_0) \cdot f_c(t) + T_0 & t_h + t_T \leq t \leq t_h + t_T + t_c \end{cases} \qquad (4)$$

. The cooling and heating functions are chosen as $f_h(t) = \sin\left(\frac{\pi}{2}\frac{t}{t_h}\right)$ with $t_h = 0.1 \cdot t_T$ and $f_c(t) = 1 - \sin\left(\frac{\pi}{2}\frac{t-(t_h+t_T)}{t_c}\right)$ with $t_c = 0.05 \cdot t_T$, respectively. Thusly constructed temperature evolution with $t_T = 600\,\text{s}$ and the temperatures taken from digitized data of the electrical recovery experiment [14], is represented in fig. 1.

3. Results

3.1. Primary knock-out events

Three symmetrically non-equivalent "atomic lenses" where identified. They are depicted as semi-translucent, yellow areas in the first row of fig. 2. The figures in the corresponding column depict the precise direction along which the central atom was shot with varying kinetic energy by means of a solid yellow arrow. Note the arrow only indicates the direction, its length does not convey any information. The kinetic energy of the recoil was increased in steps of $\geq 1.0\,\text{eV}$ along all the indicated directions.

Subsequent relaxations were carried out only, if our diagnosing scripts indicate the formation of a possible defect. The corresponding criterion is at least one atom being displaced from its initial, perfect lattice site by more than half a lattice parameter at the end of the ab-initio molecular dynamics (AIMD) simulation. Most of the time, a rather widely separated Frenkel pair of a basal-octahedral (BO) interstitial atom and a vacancy emerge. On two occasions however, closely correlated pairs of a vacancy and an interstitial atom in a site distinct from BO
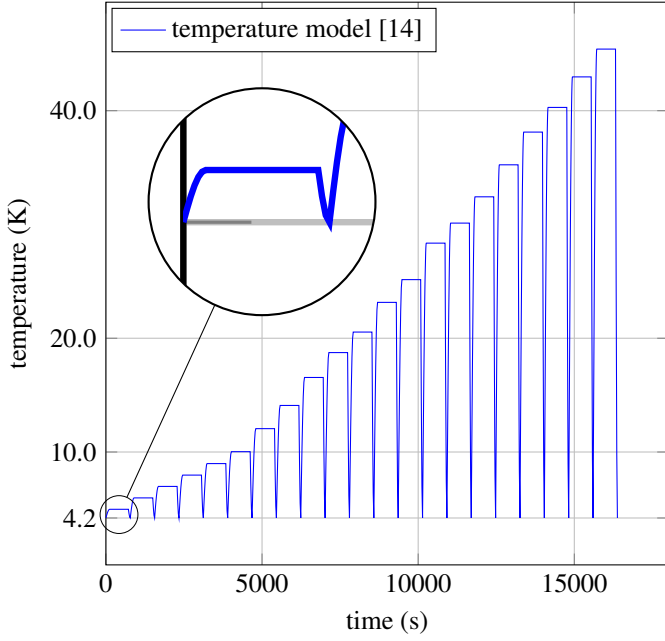
Figure 1: first heating cycles of the overall temperature function used to model experimental recovery [14].

(a) basal, 3 atom lense (B3AL)

(b) inclined, 3 atom lense (I3AL)

(c) 4 atom lense (4AL)

(d) B3AL-centered (B3AL-c) recoil

(e) I3AL-centered (I3AL-c) recoil

(f) 4AL-centered (4AL-c) recoil

(g) B3AL-vertex (B3AL-v) recoil

(h) 4AL-edge-up (4AL-eu) recoil

(i) B3AL-edge (B3AL-e) recoil

(j) 4AL-edge-down (4AL-ed) recoil

Figure 2: Visualizations of the considered "atomic lenses" in the topmost row and the associated, precise directions of the primary recoils in the corresponding column.

emerge. In both configurations, the interstitial atom is trapped between two adjacent basal planes, significantly displacing two other lattice atoms, each out of their respective basal plane. The geometry of the interstitial part of both defects resemble crowdion with different positions relative to their respective vacancy. Probing the stability of both configurations as described in section 2.2 confirmed that both are associated with a local potential energy minimum. In fig. 4 and fig. 6, the distorted beryllium lattice is indicated by bonds and lattice atoms as a hull around the vacancy at the bottom of both structures. Similarly, the interstitial atoms are framed by lattice atoms in their immediate vicinity which are connected by bonds only if they share a basal plane. A concise summary of these findings is given in table 1.

The energetics during both corresponding AIMD runs are shown in fig. 3 and fig. 5. The dotted lines indicate to what extend the system is "thermalized" by means of the kinetic energy of the fastest ion at every iteration. The solid lines represent the kinetic and the potential energy relative to the perfectly relaxed crystal structure, respectively. As the system is evolved from the perfectly relaxed crystal structure, the projectile initially is the only ion moving with the prescribed recoil energy. This is indicated by the initial agreement of the total kinetic energy and the energy of the fastest ion. Furthermore, the potential energy relative to the perfect crystal initially raises from zero while the kinetic energy drops as expected. The thick solid line indicates the actual energy conservation, being explicitly computed from the sum of both thinner solid lines, i.e. potential and kinetic energy. Relaxing the last configuration of these AIMD trajectories results in the configurations shown in fig. 4 and fig. 6.

3.2. Spontaneous and activated recombination

Energy barriers for the recombination of both closely correlated pairs of vacancy and interstitial were successfully
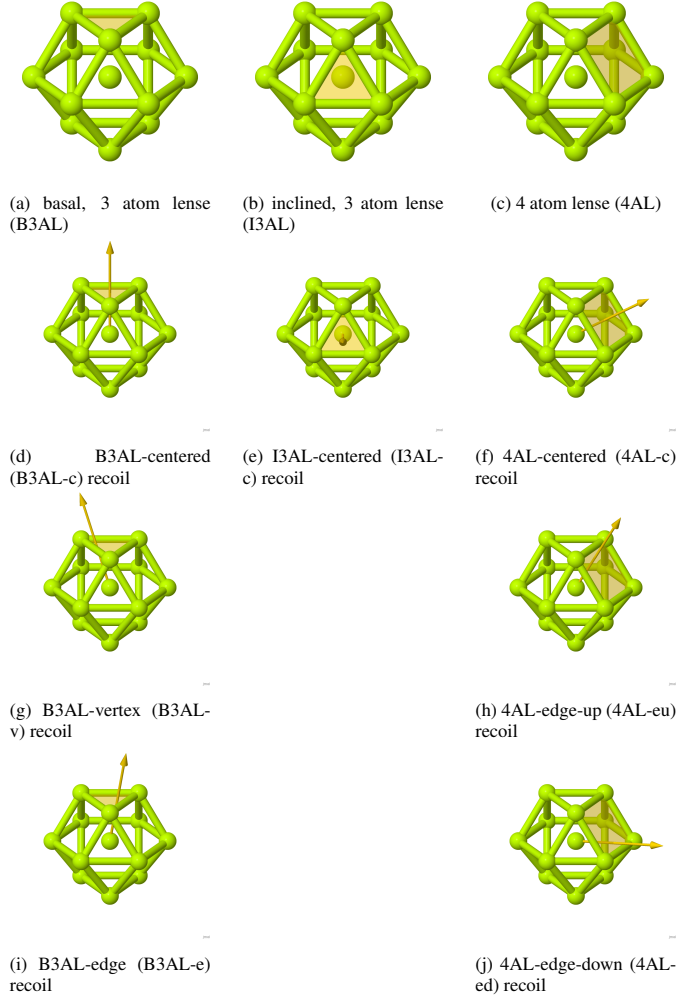
direction	threshold energy	defect
fig. 2g	17 eV	basal-octahedral, vacancy
fig. 2f	18 eV	basal-octahedral, vacancy
fig. 2j	20 eV	fig. 4
fig. 2h	22 eV	basal-octahedral, vacancy
fig. 2i	25 eV	fig. 6
fig. 2d	32 eV	basal-octahedral, vacancy
fig. 2e	34 eV	basal-octahedral, vacancy

Table 1: Summary of MD calculations considering directions, threshold energies, and defect configurations.
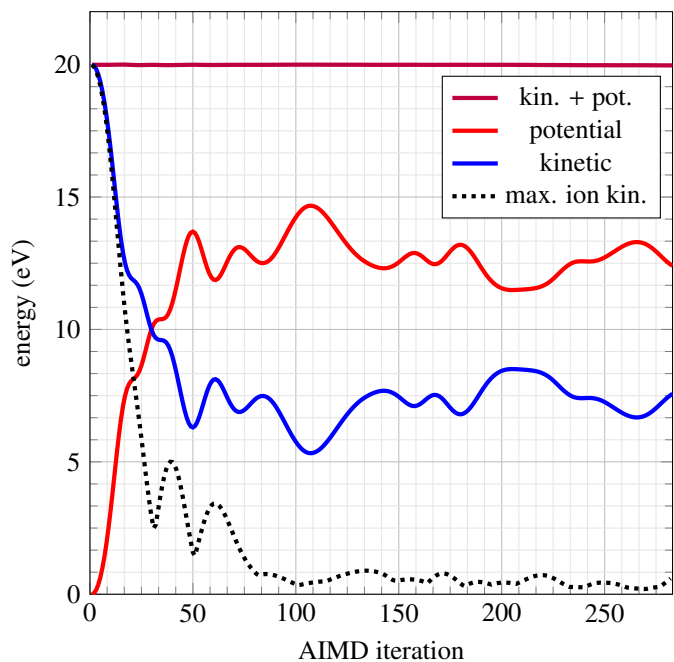
4

Figure 3: 20 eV recoil in the direction depicted in fig. 2j resulting in the defect pair shown in fig. 4.
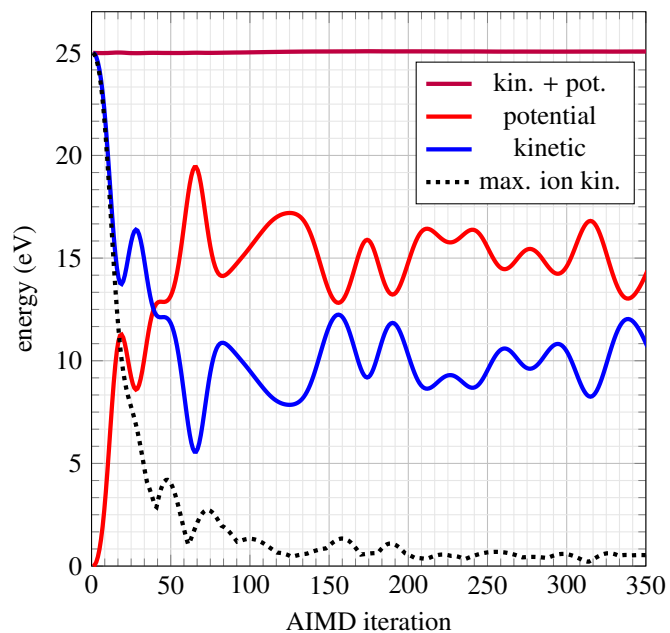

Figure 5: 25 eV recoil in the direction depicted in fig. 2i resulting in the defect pair shown in fig. 6.
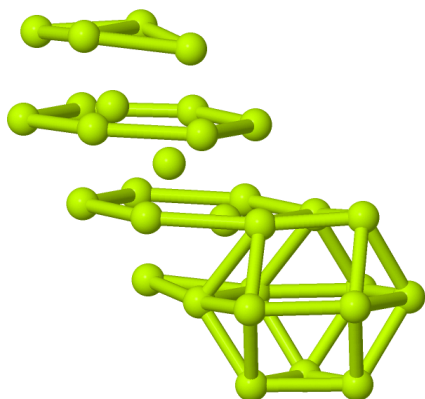

Figure 4: stable defect configuration as found by an ionic relaxation executed subsequently to an AIMD run in the direction depicted in fig. 2j.
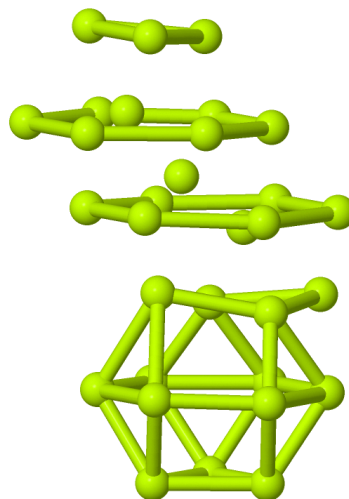

Figure 6: stable defect configuration as found by an ionic relaxation executed subsequently to an AIMD run in the direction depicted in fig. 2i.

label	basal layer Δ	ΔE
pair5.23	0	0.01 eV
20eV	n/a	0.01 eV
pair5.97	1	0.02 eV
pair5.53	1	0.03 eV
pair6.92	0	0.03 eV
pair6.54	0	0.03 eV
pair7.95	0	0.06 eV
pair6.78	1	0.07 eV
pair7.29	0	0.10 eV
25eV	n/a	0.17 eV
pair4.42	2	0.35 eV

Table 2: Summary of energy barriers associated with the recombination of interstitial and vacancy pairs depicted in fig. 9, fig. 7 and fig. 8.

obtained using our implementation of the climbing string method. The energy profiles along the MEP on the ascending side of the energy barrier versus the corresponding intermediate configurations are shown in fig. 7 and fig. 8, respectively.

Along with the two defects above, the smallest hull of stable BO interstitial positions around a single vacancy was established following the approach described at the end of section 2.2. A visualization of the resulting hull of BO interstitial atoms is given in fig. 9. Figure 9a consists of the "intra-layer" part of the hull comprising closely correlated pairs of vacancy and BO interstitials residing in the same basal plane. Figure 9b additionally shows the "inter-layer" part of the hull comprising closely correlated pairs of vacancy and BO interstitials spanning two directly adjacent basal planes. Generally, for vacancies and BO interstitials in Frenkel pairs spanning layers not directly adjacent to another, no spontaneous recombination is observed. Thus, fig. 9 already conveys the full geometric information concerning the hull delimiting the spontaneous recombination volume due to the stacking order inherent to the Be crystal. The energy barriers for recombination processes associated with Frenkel pairs in the hull, the two post-MD configurations, as well as one pair spanning further than directly adjacent basal planes are summarized in table 2, ordered by increasing energy.

3.3. A simple recovery model

A simple recovery model of all defects summarized in table 2 as completely independent entities is automatically derived as explained in section 2.4. To that end, vertices representing concentrations $\vec{c}$ of all the defects in table 2 as well as just-recovered defects are considered. Edges representing the rates of recovery as described within the general context in eq. (2) are added for every row. These rates are given as some particular instances of eq. (2), generally following the pattern of a quadruple product

$$P(\text{defect}) \cdot M(\text{process}) \cdot \nu \cdot P(\Delta E, T) \qquad (5)$$

with the probability of a randomly sampled lattice site being part of a given defect $P(\text{defect})$, the symmetry-induced multiplicity of the considered process contributing the corresponding

rate $M(\text{process})$, the attempt frequency of the process ν, and the probability of success $P(\Delta E, T)$ for given activation energy ΔE and temperature T. Thus, with $P(\text{defect})$ approximated by simple concentrations, $\nu = 10^{13}$ Hz, ΔE from the corresponding column of table 2, and $T(t)$ as shown in fig. 1, all recovery processes can be implemented consistently. Note that only one distinct energy barrier into the spontaneous recombination volume per defect is considered in all cases. Although there are cases where more than one symmetrically distinct process could result in a recombination, they are expected to be associated with very similar barriers.

In a summarizing example, the first row of table 2 is associated with an edge from vertex "pair5.23" to vertex "recovered", contributing the rate of "pair5.23" defect recovery

$$r_{\text{pair5.23}\rightarrow\text{recovered}}(\vec{c}, t) = \underbrace{c_{\text{pair5.23}}}_{P(\text{defect})} \cdot \overbrace{4}^{M(\text{process})} \cdot \underbrace{10^{13}\,\text{Hz}}_{\nu} \cdot \overbrace{\exp\left(-\frac{0.01}{k_B T(t)}\right)}^{P(\Delta E, T)}$$

to the model. After adding rates for the rest of the rows in table 2, eq. (3) gives rise to an ODE system of the whole recovery model. Solving the resulting ODE system of this particular model with initial concentrations $\vec{c}_0$ of 0.01 for each defect in table 2 and 0.0 for the special "recovered" vertex, results in the solution depicted in fig. 10. Figure 10a shows the evolution of the considered concentrations with time during the experiment, i.e while the temperature function consisting of the series of heat cycles like eq. (4), the beginning of which is depicted in fig. 1, is applied. While this quantity generally cannot be observed directly in experiment, the recovery spectrum resulting from finite differences of electrical resistivity measurements after subsequently completed heating cycles is expected to be roughly proportional to the amount of recovering defects. Thus, fig. 10b shows the ODE solution discretized correspondingly as a thick line along with the digitized experimental [14] values taken from the empty circles of Fig. 3 in the provided reference.

3.4. An advanced recovery model

The simple model assumes that all defects decay independently from each other. A more realistic recovery model introduces intra-layer diffusion of self-interstitials, allowing for the transformation of defects into another. This occures by dissociation of closely correlated pairs and formation of other closely correlated pairs. The result of the dissociation of a closely correlated pair is a generic Frenkel pair where interstial and vacancy are located further apart from each other. To incorporate such pairs into the recovery model, another special vertex "frenkel" is added. Interactions are considered in terms of additional edges between one of the vertices representing the defects in table 2 and the new vertex "frenkel". Outgoing edges at vertex "frenkel" represent the creation of closely correlated pairs at the expense of the concentration of non-correlated Frenkel pairs, while incoming edges represent the respective dissociation.

Generally, all rates associated with these additional edges again follow the quadruple product formulation of eq. (5). The

(a) energy profile sketch

(b) minimum   (c) 1st MEP configuration   (d) 2nd MEP configuration   (e) 3rd MEP configuration   (f) saddle point
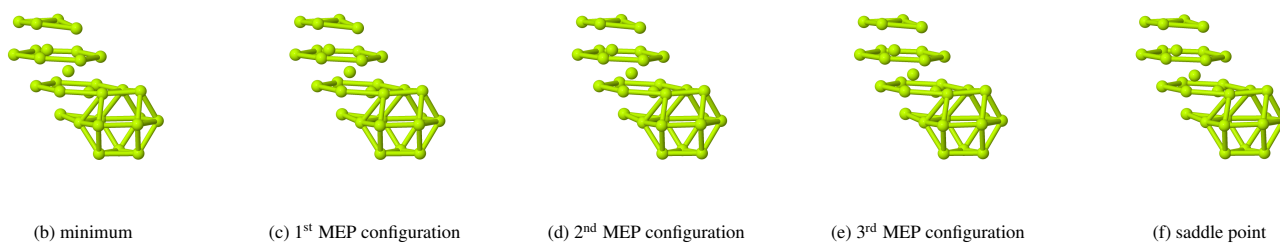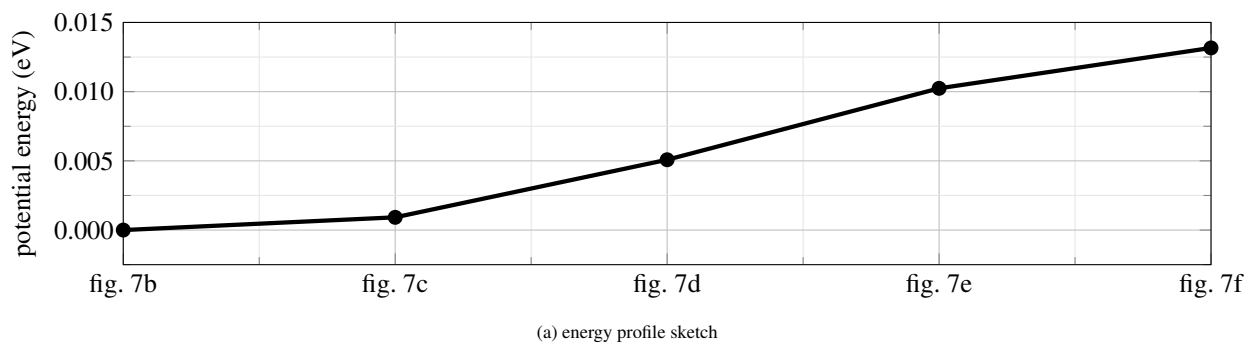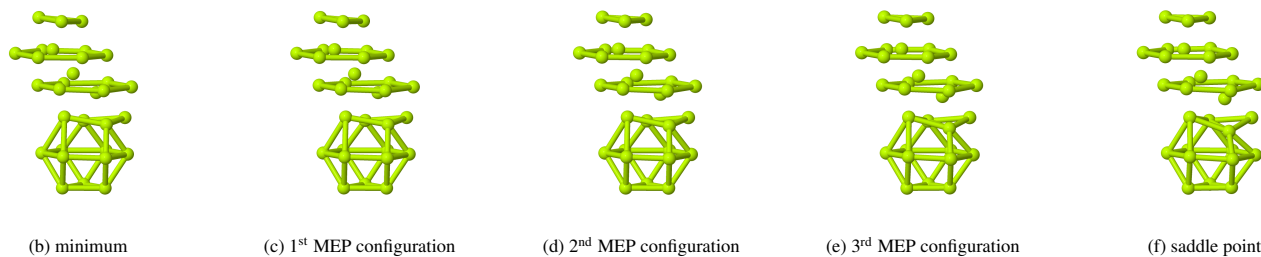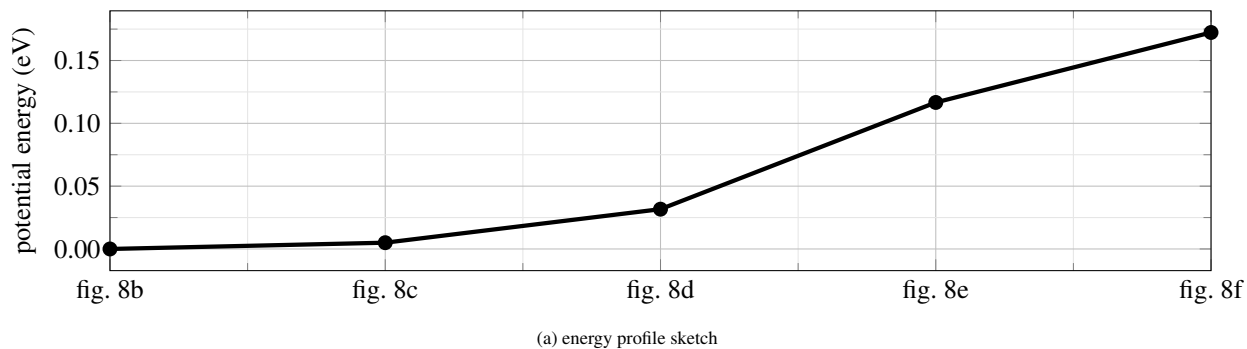
Figure 7: Visualization of the MEP on the energy ascending side of the recombination barrier out of the configuration in fig. 4.

(a) energy profile sketch

(b) minimum   (c) 1st MEP configuration   (d) 2nd MEP configuration   (e) 3rd MEP configuration   (f) saddle point
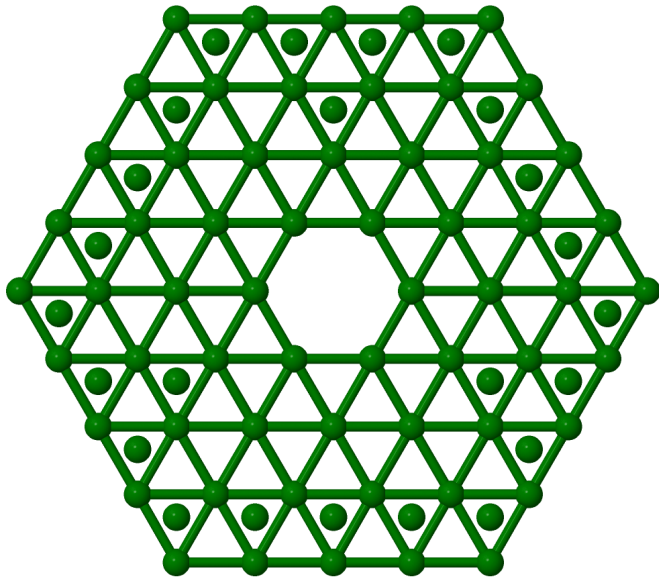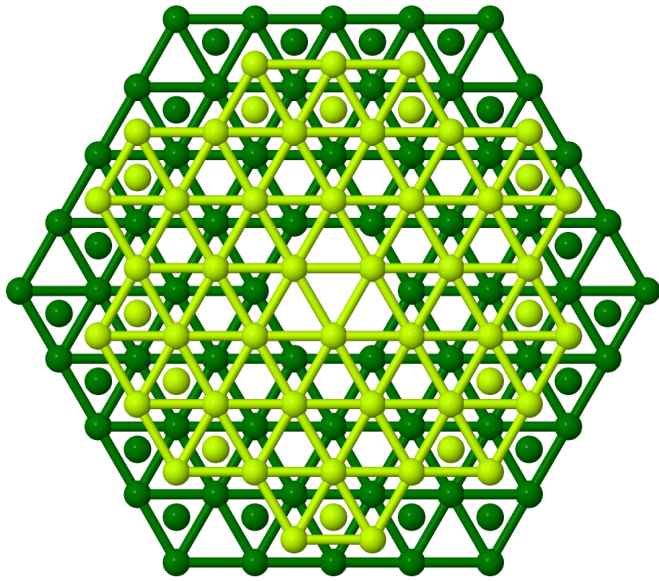
Figure 8: Visualization of the MEP on the energy ascending side of the recombination barrier out of the configuration in fig. 6.
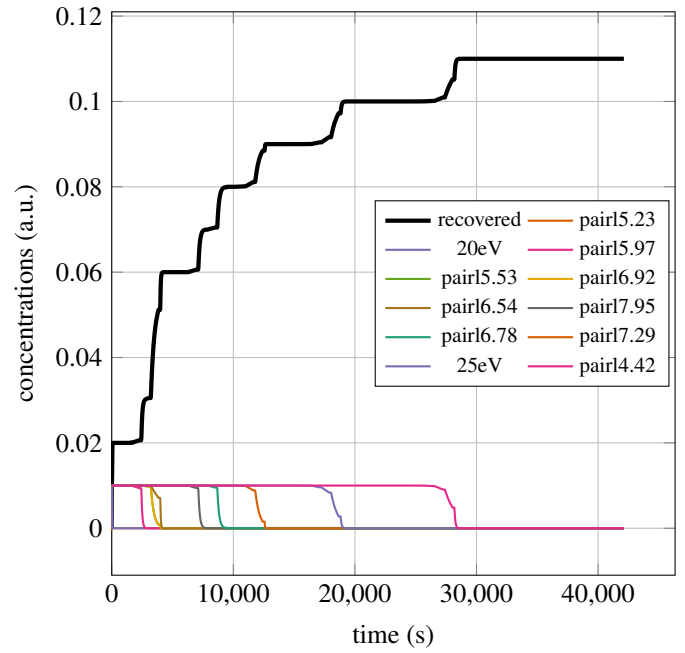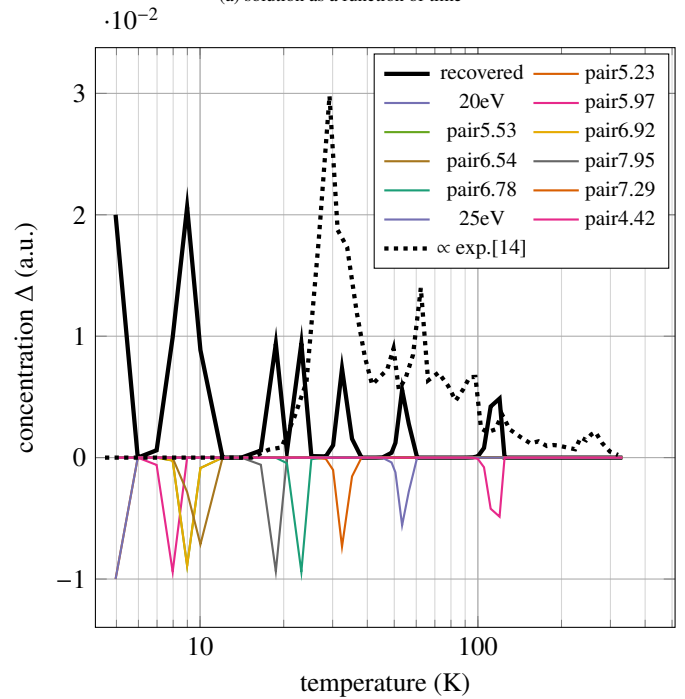
(a) intra-layer configurations

(b) inter-layer configurations

Figure 9: Visualization of the hull of stable basal-octahedral interstitials delimiting the volume of spontaneous recombination.

(a) solution as a function of time

(b) discretized to experimental [14] holding temperatures as in fig. 1

Figure 10: Solution of the ODE system corresponding to a recovery model of independent defects as summarized in table 2.

barrier for dissociation of "pair6.54" and "pair5.97" defects were calculated as examples of dissociating inter- and intra-layer pairs using the climbing string method as described in section 2.3. With barriers of 0.115 eV and 0.125 eV respectively, both turn out to be very close to the intra-layer Be self-interstitial diffusion barrier of 0.12 eV [25]. Therefore, the corresponding barriers for creation and dissociation of all remaining defects in table 2 are approximated by the barrier of free intralayer diffusion of self-interstitials with 0.12 eV. This introduces creation rates of closely correlated pairs like

$$
r_{\text{Frenkel}\rightarrow\text{pair7.95}}(\vec{c}, t) = \underbrace{(c_{\text{Frenkel}})^2}_{P(\text{defect})} \cdot \overbrace{3 \cdot 6}^{M(\text{process})} \cdot \underbrace{10^{13}\,\text{Hz}}_{\nu} \cdot \overbrace{\exp\left(-\frac{0.12}{k_B T\,(t)}\right)}^{P(\Delta E, T)}
$$

for the closely correlated pair defect "pair7.95" at the six corners of the hexagonal shape of intra-layer BO interstitial paris in fig. 9a and analogous rates for all the remaining rows in table 2, adhering to the pattern in eq. (5). The probability of finding suitable pairs of an interstitial and vacancy, represented as a squared concentration, can be understood as follows. As interstitials and vacancies can only recombine pairwise, their respective overall concentration is always the same and each Frenkel pair consists of one vacancy and interstitial, thus the probability to find a vacancy (or, alternatively, a BO interstitial) at a given lattice site is approximated by c_{Frenkel} as well. The same can be said for arbitrary sites right beyond the hull of the volume of spontaneous recombination around a vacancy, and thus finding both, a BO interstitial and a vacancy, simultaneously can be approximated by c_{Frenkel}^2. The multiplicity factor accounts for the fact that there are three actual intra-layer BO interstitial sites from which the diffusion step might occur at each of the six corners of the hexagon in fig. 9a. The corresponding dissociation rates leading to the formation of Frenkel pairs follow analogously, e.g.

$$
r_{\text{pair7.95}\rightarrow\text{Frenkel}}(\vec{c}, t) = \underbrace{c_{\text{pair7.95}}}_{P(\text{defect})} \cdot \overbrace{3}^{M(\text{process})} \cdot \underbrace{10^{13}\,\text{Hz}}_{\nu} \cdot \overbrace{\exp\left(-\frac{0.12}{k_B T\,(t)}\right)}^{P(\Delta E, T)}
$$

for the closely correlated pair defect at a distance of 7.95 Å at any of the six corners of the hexagon in fig. 9a.

Note that fig. 10b suggests the defects up to including "pair6.78" in table 2 recombine before the recovery experiment even starts due to their very low activation energies. This explains the absence of corresponding peaks in the experimentally measured spectrum. Therefore, the initial concentrations of those defects and the "recovered" vertex are chosen to be 0.0 and those of "pair7.29", "25eV", "pair4.42" and "Frenkel" are initialized to 0.01. Solving the ODE system of this model derived via eq. (3) for the initial concentrations mentioned before results in the temperature-discretized solution shown in fig. 11.
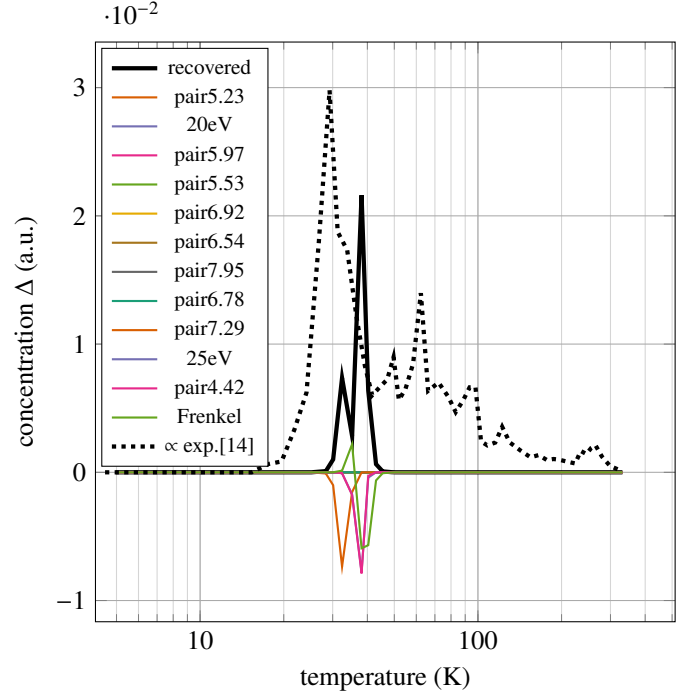

Figure 11: Temperature-discretized solution of the ODE system corresponding to the refined recovery model including intra-layer diffusion.

4. Discussion

The *ab initio* molecular dynamics (AIMD) calculations carried out emphasize that the principal self-interstitial position in beryllium is basal-octahedral (BO), as only two exceptions of all defect-producing AIMD calculations resulted in closely correlated pairs different from a vacancy and BO interstitial at varying distances. Naturally, we can not rule out there are further, as of now overlooked, closely correlated pairs, as our sampling of the directional search space is restricted to the small set of directions depicted in fig. 2 and is therefore rather rough. In principal, even slight deviations of a particular direction may lead to significantly different trajectories and thus end up generating very different defect structures. The highest threshold displacement energy (TDE) estimations of 32 eV and 34 eV, as summarized in table 1, are associated with recoils in high symmetry directions right through the center of the "atomic lenses" depicted in fig. 2d and fig. 2e, respectively. At the same time, the recoil right through the center of the remaining "atomic lense", depicted in fig. 2f, is associated with a comparatively low TDE of just 18 eV. This corresponds to the overall size of the lenses, the smaller of which being delimited by just 3 atoms and the larger one by four. The key property of stable Frenkel pairs emerging from low-TDE recoils is a large separation along the c axis, while the separation in the other two crystallographic directions is smaller. With the distances of closely correlated pairs summarized in table 2, it can be deduced that the volume of spontaneous recombination has the approximate shape of an oblate spheroid with an equatorial radius of approximately 8.0 Å and a distance of 4.4 Å from center to pole. These findings already hint to a pronounced anisotropy of the
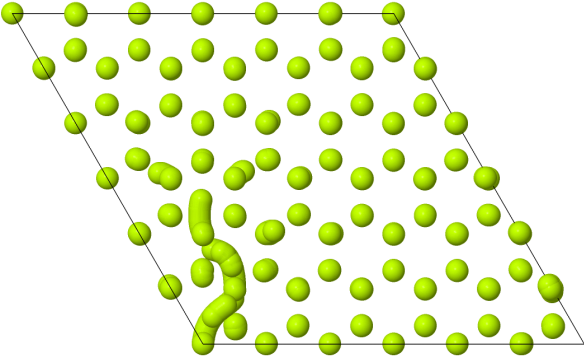
Figure 12: Overlay of all configurations the system passes along the minimal energy path during the recombination process of an intra-layer Frenkel pair.

volume around a vacancy within which spontaneous recombination takes place and outside of which stable Frenkel pairs can be formed. Indeed, the laterally more remote BO interstitials after higher energy TDE recoils generally reside in the same or directly adjacent basal layers, outside of the volume of spontaneous recombination which is significantly larger within basal planes.

At this point, we consider the thermally activated recombination of closely correlated pairs delimiting the volume of spontaneous recombination as shown in fig. 9. After overcoming the associated barriers, recombination from the hull over the extensive distances involved takes place by chain-like processes of substituting neighboring lattice atoms, with the last atom dropping into the vacancy. Figure 12 shows an example of such a process for the recombination of the "pair5.23" defect. This overlay visualizes all configurations the system passes through when descending in energy along the minimal energy path right beyond the saddle point until the vacancy at the corner of the simulation cell is filled.

Generally, both recovery models considered in section 3.3 and section 3.4 contain some additional uncertainty from the unknown details of temperature evolution during heating and cooling within the given experimental setup [14]. While the holding temperature levels were readily reproduced from digitized data out of the respective plot from the reference above and the holding time at each temperature were given as 600 s as well, the heating and cooling phases were not described in detail. We chose some plausible heating and cooling periods of, respectively, 60 s and 30 s, during which the temperature is ramped up and down according to some typical function as described in eq. (4). Slower, and thus longer, cooling and heating phases, generally lead to a shift of the resulting peaks to lower temperatures. Depending on the effective heating power of the experimental setup, this shift may be more or less pronounced at high or low temperatures.

Another shift of all peaks independent from the applied holding temperature could result from the chosen attempt frequency ν in eq. (5). As the considered process rates within the model scale linearly with this quantity, it is immediately obvious that underestimation will result in shifts to higher temperatures and vice versa. The typical choice of 10^{13} Hz used in this work may be an underestimation considering beryllium atoms have a comparatively small mass, resulting in an artificial peak shift to higher temperatures.

With that in mind, it is noted that the three latest simulated peaks of the "pair7.29", "25eV", and "pair4.42" defects appearing well within the experimentally observed spectrum in fig. 10b consistently show up just behind of experimental peaks. However, due to the rich structure of the experimentally observed peaks, this could be said for almost every peak position. Thus, we do not consider this a convincing mapping of experimental peaks to modeled processes. Figure 10b indicates that the first and principal experimentally observed peak is not due to the closely correlated defects summarized in table 2 though. Clearly, the peaks associated with defects in table 2 up to and including "pair6.78" recover significantly too early to directly contribute to this peak. Therefore, we deduce those closely correlated defects recover almost immediately if they were created from recoil events. We reckon this might point out a systematic shortcoming of simulating this very last stage of the full cascade in an isolated manner. This approach does not account for any additional energy deposited from preceding events of the same subcascade in the very lattice regions of the closely correlated pairs. Of course, under irradiation, an increased local temperature due to cascade events would result in an immediate recombination of such defects, thus excluding their observation in subsequent resistivity recovery experiments.

Taking fast intra-layer selfinterstitial diffusion into account radically alters the simulated spectrum as can be seen from comparing fig. 11 with fig. 10b. All the peaks associated with defects of non-zero initial defect configurations, namely the "pairl7.29", "25eV", "pair4.42", and generic "Frenkel" types, now indirectly contribute to one principal peak which appears in our model at higher temperatures than in the experimental outcome. This is due to fundamentally new dynamics taking place. Instead of recombining with their own nearest vacancies, the interstitial atoms now become mobile within their respective basal layer. That way, interstitials can travel within this layer until they hit a hull delimiting spontaneous recombination around another vacancy. Almost all the recombination barriers from that hull are significantly lower than the intra-layer diffusion barrier of 0.12 eV. The closely correlated pairs associated with such low recombination barriers will be now formed again as the result of diffusion within basal planes. Our model captures the effects from the reemergence of such closely correlated pair, as can be seen when considering the changes in the defect concentrations in fig. 11 in detail. The onset of the simulated recovery peak is clearly associated with direct recovery of "pairl7.29" defects overcoming the respective recombination energy barrier of 0.102 eV. This is apparent when noting the initial perfect symmetry between the negative orange peak of the change in "pair7.29" concentration and the thick black posi-

tive recovery peak. At slightly higher temperatures, the intra-layer interstitial diffusion sets in and as a result our model accounts for a corresponding increase in the generic "Frenkel" defect concentration, cf. light green positive peak. This increase is facilitated by a corresponding drop in the concentrations of the closely correlated pair defects with recombination barriers above 0.12 eV as their diffusive dissociation sets in. This process additionally adds to the recovery peak as the temporarily increased generic "Frenkel" defect concentration is simultaneously absorbed by all recombination processes with smaller barriers as summarized in table 2. In the following heating cycles, this concentration flow pattern continues and leads to the emergence of the principle recovery peak just before 40 K. The leading peak feature at the principle peak of the simulated spectrum could be due to the incomplete set of recombining closely correlated pairs as their collective recovery rate contributions are what depletes the "Frenkel pair" concentration which does show a temporary increase. Unfortunately, an exhaustive search for such defects currently is unfeasible based on DFT calculations. This suggests the following interpretation of the experimental principal peak. While the bulk of the principal peak is likely composed from additional closely correlated pairs recombining with barriers slightly below the 0.1 eV of "pair7.29" defects, a contribution from fast intra-layer self-interstitial diffusion could explaining the shoulder in the experimental spectrum.

It is important to note that this study can only be expected to reproduce features inherent to a perfect single crystal without additional sinks for vacancies and BO interstitials. Although obstacles like impurities, lattice defects, etc. can in principal be considered on the exact same footing within the more general scope of our rate-based approach, costly additional computations are necessary to find the corresponding energy barriers. Our results suggest that the rich structure in the experimental spectrum right after the very first peak that are not reproduced by our model might be entirely due to imperfections like these. Therefore, it would be interesting to compare recovery spectra of different specimens with impurity contents vastly different from the reported [14] 99.9 % of the considered experiment.

If our interpretation of fast intra-layer diffusion and recombination contributing to the experimentally observed principal recovery peak in beryllium is correct, a similar concordance is expected for other hcp materials with similar ratios of $\frac{c}{a} < \sqrt{8/3}$. One such candidate, for which the corresponding intra-layer self interstitial diffusion barrier of 0.34 eV was computed along with that of Be in a different context [25], is Zr. Corresponding electrical resistivity recovery data on Zr has been published [26]. Thus, a corresponding minimal recombination model considering only generic "Frenkel" pair defects and similarly fast recombination from a supposedly similar spontaneous recombination hull was derived on the same footing as explained for the models concerning beryllium earlier. Within this model, a total initial "Frenkel" pair concentration of 0.01 produces a good correlation with the experimental principal recovery peak of Zr, see fig. 13. Despite Zr seemingly retains some closely correlated defects recovering at sig-
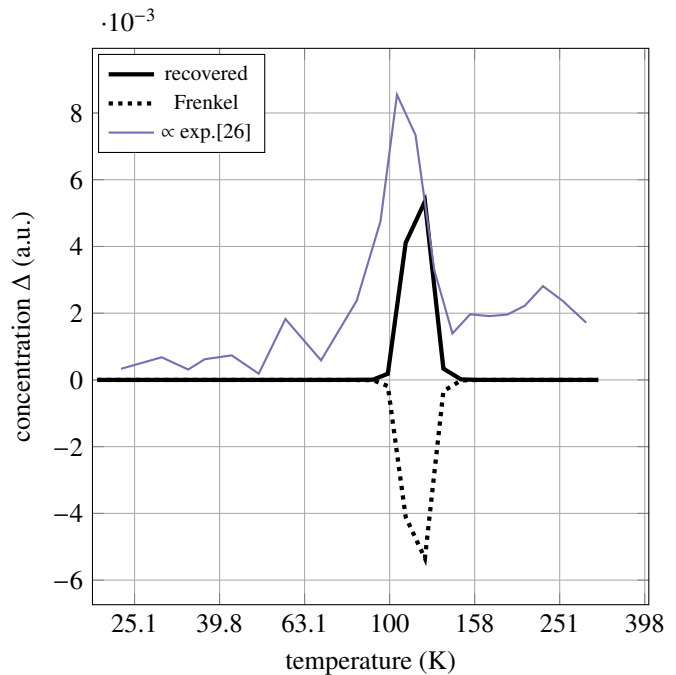

Figure 13: Temperature-discretized solution and experimental data [26] of the simple recovery model for Zr.

nificantly lower temperatures than the principal recovery peak, the agreement of this simple model for recovery and the experimental data clearly suggest our conjectured attribution is correct. We can suggest that the onset of long-range diffusion along the c-axis will not result in an additional electrical resistivity recovery peak, as only the fastest process is responsible for the recovery. Further peaks at higher temperatures can be attributed to the release of interstitials bound by obstacles, which are inevitable in real specimens. Generally, our findings suggest that the spectra at temperatures beyond those of the principal recovery peak needs to be explained by traps, e.g. impurities, hindering mobility of self-interstitials and vacancies until higher temperatures.

5. Conclusions

The principal self-interstitial site for Be, even for closely correlated pairs, seems to be in the basal-octahedral (BO) coordination with low energy barriers for the recombination of closely correlated BO self-interstitials and vacancy pairs. The spontaneous recombination hull in Be roughly forms an oblate spheroid in the basal plane with an equatorial radius of approximately 8.0 Å and a distance of 4.4 Å from center to pole.
The multi-scale rate-based model of electric resistivity recovery based on *ab initio* computations and incorporating all the findings above suggests the recombination of closely correlated pairs alone does not account for the distinct first peak in the recovery spectra of beryllium. With most closely correlated pairs already annealed again just after creation during irradiation, the principal electrical recovery peak of Be is suggested to be supported by the onset of fast intra-layer self-interstitial diffusion

on basal planes as well. An expected similar agreement between the onset of basal intra-layer self-interstitial diffusion in similar hcp metals was successfully confirmed by means of a minimal model on equal footing for Zr as an example. Our findings suggest that the principal peak of electrical resistivity recovery spectra in other hcp metals is not exclusively caused by recombination of closely correlated pairs, but also contains contributions from the onset of fast intra-layer self-interstitial diffusion. They also imply that the spectra at temperatures beyond those of the principal recovery peak needs to be explained by traps hindering mobility of self-interstitials and vacancies until higher temperatures.

6. Acknowledgements

References

[1] K. Ioki, V. Barabash, A. Cardella, F. Elio, Y. Gohar, G. Janeschitz, G. Johnson, G. Kalinin, D. Lousteau, M. Onozuka, R. Parker, G. Sannazzaro, R. Tivey, Journal of Nuclear Materials 258–263, Part 1 (1998) 74 – 84. URL: http://www.sciencedirect.com/science/article/pii/S0022311598003560. doi:http://dx.doi.org/10.1016/S0022-3115(98)00356-0.

[2] Y. Poitevin, L. Boccaccini, M. Zmitko, I. Ricapito, J.-F. Salavy, E. Diegele, F. Gabriel, E. Magnani, H. Neuberger, R. Lässer, L. Guerrini, Fusion Engineering and Design 85 (2010) 2340 – 2347. URL: http://www.sciencedirect.com/science/article/pii/S0920379610004254. doi:http://dx.doi.org/10.1016/j.fusengdes.2010.09.027, proceedings of the Ninth International Symposium on Fusion Nuclear Technology.

[3] P. Vladimirov, D. Bachurin, V. Borodin, V. Chakin, M. Ganchenkova, A. Fedorov, M. Klimenkov, I. Kupriyanov, A. Moeslang, M. Nakamichi, T. Shibayama, S. V. Til, M. Zmitko, Fusion Science and Technology 66 (2014) 28 – 37. doi:http://dx.doi.org/10.13182/FST13-776.

[4] M. Klimenkov, V. Chakin, A. Moeslang, R. Rolli, Journal of Nuclear Materials 443 (2013) 409 – 416. URL: http://www.sciencedirect.com/science/article/pii/S0022311513009380. doi:http://dx.doi.org/10.1016/j.jnucmat.2013.07.050.

[5] V. P. Chakin, A. O. Posevin, R. N. Latypov, Atomic Energy 101 (2006) 743–749. URL: http://dx.doi.org/10.1007/s10512-006-0162-9. doi:10.1007/s10512-006-0162-9.

[6] M. Norgett, M. Robinson, I. Torrens, Nuclear Engineering and Design 33 (1975) 50 – 54. URL: http://www.sciencedirect.com/science/article/pii/0029549375900357. doi:http://dx.doi.org/10.1016/0029-5493(75)90035-7.

[7] J. Biersack, J. Ziegler, M. Ziegler, SRIM Co (2008).

[8] K. Nordlund, J. Wallenius, L. Malerba, Nuclear Instruments and Methods in Physics Research Section B: Beam Interactions with Materials and Atoms 246 (2006) 322 – 332. URL: http://www.sciencedirect.com/science/article/pii/S0168583X06000243. doi:http://dx.doi.org/10.1016/j.nimb.2006.01.003.

[9] P. Olsson, C. S. Becquart, C. Domain, Materials Research Letters 4 (2016) 219–225. URL: http://dx.doi.org/10.1080/21663831.2016.1181680. doi:10.1080/21663831.2016.1181680. arXiv:http://dx.doi.org/10.1080/21663831.2016.1181680.

[10] N. Juslin, K. Nordlund, J. Wallenius, L. Malerba, Nuclear Instruments and Methods in Physics Research Section B: Beam Interactions with Materials and Atoms 255 (2007) 75 – 77. URL: http://www.sciencedirect.com/science/article/pii/S0168583X06010688. doi:http://dx.doi.org/10.1016/j.nimb.2006.11.046, computer Simulation of Radiation Effects in SolidsProceedings of the Eighth International Conference on Computer Simulation of Radiation Effects in Solids (COSIRES 2006)Computer Simulation of Radiation Effects in Solids.

[11] P. Vladimirov, V. Borodin, Nuclear Inst. and Methods in Physics Research, B 393 (2017) 195–199. doi:10.1016/j.nimb.2016.09.027.

[12] F. Maury, P. Vajda, A. Lucasson, P. Lucasson, Phys. Rev. B 8 (1973) 5496–5505. URL: http://link.aps.org/doi/10.1103/PhysRevB.8.5496. doi:10.1103/PhysRevB.8.5496.

[13] F. Maury, P. Vajda, A. Lucasson, P. Lucasson, Phys. Rev. B 8 (1973) 5506–5518. URL: http://link.aps.org/doi/10.1103/PhysRevB.8.5506. doi:10.1103/PhysRevB.8.5506.

[14] J. Delaplace, J. C. Nicoud, D. Schumacher, G. Vogl, physica status solidi (b) 29 (1968) 819–824. URL: http://dx.doi.org/10.1002/pssb.19680290233. doi:10.1002/pssb.19680290233.

[15] W. Ren, E. Vanden-Eijnden, The Journal of Chemical Physics 138 (2013) 134105. URL: http://dx.doi.org/10.1063/1.4798344. doi:10.1063/1.4798344. arXiv:http://dx.doi.org/10.1063/1.4798344.

[16] G. Kresse, J. Hafner, Phys. Rev. B 47 (1993) 558–561. URL: http://link.aps.org/doi/10.1103/PhysRevB.47.558. doi:10.1103/PhysRevB.47.558.

[17] G. Kresse, J. Furthmüller, Phys. Rev. B 54 (1996) 11169–11186. URL: http://link.aps.org/doi/10.1103/PhysRevB.54.11169. doi:10.1103/PhysRevB.54.11169.

[18] S. P. Ong, W. D. Richards, A. Jain, G. Hautier, M. Kocher, S. Cholia, D. Gunter, V. L. Chevrier, K. A. Persson, G. Ceder, Computational Materials Science 68 (2013) 314 – 319. URL: http://www.sciencedirect.com/science/article/pii/S0927025612006295. doi:http://dx.doi.org/10.1016/j.commatsci.2012.10.028.

[19] P. E. Blöchl, Phys. Rev. B 50 (1994) 17953–17979. URL: http://link.aps.org/doi/10.1103/PhysRevB.50.17953. doi:10.1103/PhysRevB.50.17953.

[20] G. Kresse, D. Joubert, Phys. Rev. B 59 (1999) 1758–1775. URL: http://link.aps.org/doi/10.1103/PhysRevB.59.1758. doi:10.1103/PhysRevB.59.1758.

[21] J. P. Perdew, Y. Wang, Phys. Rev. B 45 (1992) 13244–13249. URL: http://link.aps.org/doi/10.1103/PhysRevB.45.13244. doi:10.1103/PhysRevB.45.13244.

[22] M. Methfessel, A. T. Paxton, Phys. Rev. B 40 (1989) 3616–3621. URL: http://link.aps.org/doi/10.1103/PhysRevB.40.3616. doi:10.1103/PhysRevB.40.3616.

[23] A. A. Hagberg, D. A. Schult, P. J. Swart, in: Proceedings of the 7th Python in Science Conference (SciPy2008), Pasadena, CA USA, pp. 11–15.

[24] E. Jones, T. Oliphant, P. Peterson, et al., SciPy: Open source scientific tools for Python, 2001–. URL: http://www.scipy.org/, [Online; accessed ¡today¿].

[25] P. V. Vladimirov, M. G. Ganchenkova, V. A. Borodin.

[26] S. Takamura, M. Kobiyama, Radiation Effects 49 (1980) 247–250. URL: https://doi.org/10.1080/00337578008237489. doi:10.1080/00337578008237489. arXiv:https://doi.org/10.1080/00337578008237489.